GEOPHYSICS, VOL. 83, NO. 5 (SEPTEMBER-OCTOBER 2018); P. R389–R400, 15 FIGS.
10.1190/GEO2017-0571.1

Site characterization with 3D elastic full-waveform tomography

Trung Dung Nguyen[1] and Khiem T. Tran[2]

ABSTRACT

We have developed a 3D elastic full-waveform inversion (FWI) method for geotechnical site characterization. The method is based on a solution of 3D elastic-wave equations for forward modeling to simulate wave propagation and a local optimization approach based on the adjoint-state method to update the model parameters. The staggered-grid finite-difference technique is used to solve the wave equations together with implementation of the perfectly matched layer condition for boundary truncation. Seismic wavefields are acquired from geophysical testing using sensors and sources located in uniform 2D grids on the ground surface, and they are then inverted for the extraction of 3D subsurface wave velocity structures. The capability of the presented FWI method is tested on synthetic and field data sets. The inversion results from synthetic data indicate the ability of characterizing laterally variable low- and high-velocity layers. Field experimental data were collected using 96 receivers and a propelled energy generator to induce seismic wave energy. The field data result indicates that the waveform analysis was able to delineate variable subsurface soil layers. The seismic inversion results are generally consistent with invasive standard penetration test *N*-values, including identification of a low-velocity zone.

INTRODUCTION

Site characterization is important for successful design of substructures because unanticipated site conditions such as highly variable soil/rock layers with embedded low-velocity anomalies (soft soils) cause significant problems during and after the construction of foundations. Surface-based seismic methods are often used for geotechnical site characterization to assess spatial variation and material properties. They include surface wave, refraction tomography, and full-waveform tomography methods. Surface-wave methods such as multichannel analysis of surface waves (Park et al., 1999) use the dispersive characteristics of Rayleigh waves to determine 1D S-wave velocity V_S profiles. This method tends to average V_S values over considerable volumes of material, and it is not very sensitive to thin embedded low-velocity layers. Refraction tomography uses the first-arrival times to determine P-wave velocity V_P profiles. Because the first-arrival signals tend to propagate through high-velocity layers, embedded low-velocity layers are not well-characterized.

As reviewed by Vireux and Operto (2009), by extracting information contained in the complete waveforms, the full-waveform inversion (FWI) approach offers the potential to produce higher resolution models of the subsurface structures than approaches that consider only the dispersive characteristic of Rayleigh waves or first-arrival times of body waves. The FWI approach could be used to identify and quantify embedded anomalies and characterize variable soil/rock layers because the propagation properties of seismic waves are modulated by the anomalies and layer interfaces. The V_S and V_P structures could be inverted independently to increase the credibility of characterized profiles.

Many algorithms for waveform inversion have been developed and applied to synthetic and real seismic data in large-scale (km scale) domains including 2D FWI (Pratt et al., 1998; Shipp and Singh, 2002; Ravaut et al., 2004; Cheong et al., 2006; Sheen et al., 2006; Askan et al., 2007; Brenders and Pratt, 2007; Sears et al., 2008; Brossier et al., 2010; Ben-Hadj-Ali et al., 2011; Prieux et al., 2011, 2013; Operto et al., 2013; Vigh et al., 2013; Métivier et al., 2014; Castellanos et al., 2015) and 3D FWI (Ben-Hadj-Ali et al., 2008; Epanomeritakis et al., 2008; Fichtner et al., 2009; Plessix, 2009; Sirgue et al., 2010; Vigh et al., 2011; Warner et al., 2013; Ha et al., 2015). Due to computational challenges, the 3D FWI algorithms often use acoustic modeling, therefore neglecting the elastic effects. The acoustic approximation generally performs well for marine hydrophone data, but it is limited for land seismic

Manuscript received by the Editor 25 August 2017; revised manuscript received 15 January 2018; published ahead of production 08 June 2018; published online 19 July 2018.
[1]Clarkson University, Department of Civil and Environmental Engineering, P.O. Box 5710, Potsdam, New York 13699-5710, USA. E-mail: nguyent@clarkson.edu.
[2]University of Florida, Department of Civil and Coastal Engineering, P.O. Box 5710, Potsdam, New York 13699-5710, USA. E-mail: ttk@ufl.edu.

data due to the importance of S-waves (Butzer et al., 2013), and thus it cannot be used for geotechnical site investigation. Studies on elastic 3D FWI are still rare.

At long propagation distances, surface waves can well separate from body waves and be removed from the inversion process. However, at a smaller length scale (0–100 m), it is difficult to separate body waves from surface waves. Only a small number of studies involved body and surface waves for near-surface investigations including 2D FWI on synthetic data (Gélis et al., 2007; Romdhane et al., 2011) and real seismic data (Tran and McVay, 2012; Bretaudeau et al., 2013; Kallivokas et al., 2013; Tran et al., 2013; Köhn et al., 2016; Nguyen et al., 2016; Sullivan et al., 2016; Tran and Luke, 2017), and 3D FWI on synthetic data (Butzer et al., 2013; Fathi et al., 2015) and real data (Fathi et al., 2016). At small scales, inherent challenges include inconsistent wave excitation, strong attenuation, strong variability of near-surface soil/rock lithology, and poor a priori information. These challenges have prevented FWI techniques from being used routinely for geotechnical site characterization (Tran and Luke, 2017).

This paper presents a new 3D FWI method for geotechnical site characterization. The method is based on a solution of 3D elastic-wave equations for forward modeling to simulate wave propagation and a cross-adjoint gradient approach for model updating to extract material property. The seismic wavefields are acquired from geophysical testing using receivers and sources located in uniform 2D grids on the ground surface and then inverted for the extraction of 3D subsurface wave velocity structures. For demonstration, the presented method was tested on synthetic data generated from a realistic subsurface profile with variable high- and low-velocity soil layers. It was also applied to field experimental data collected at a Florida test site, and FWI results are compared with invasive SPT N-values for verification.

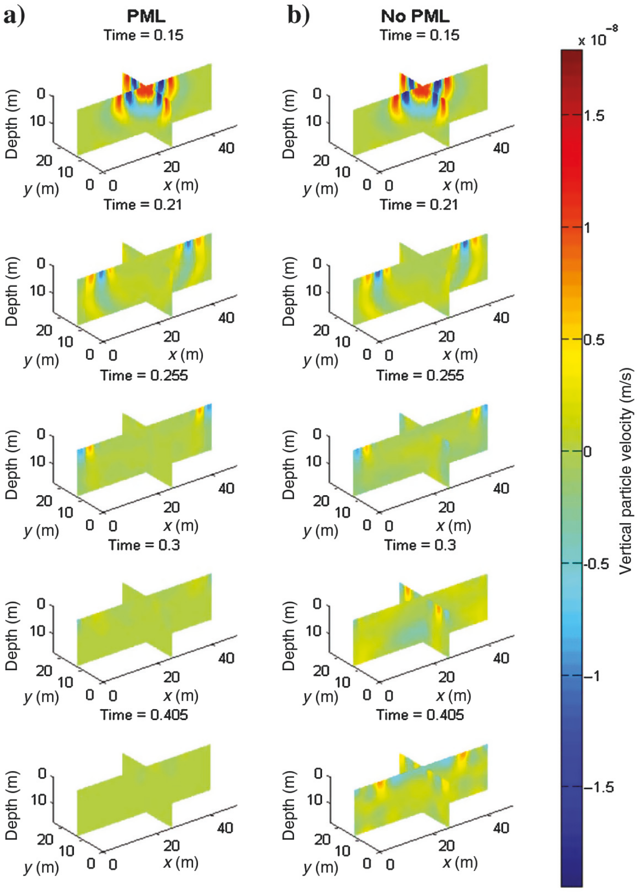

Figure 1. The 3D wave propagation with and without the PML boundary truncation.

FWI METHODOLOGY

The presented 3D FWI method includes forward modeling to generate synthetic wavefields, as well as the use of the adjoint gradient method to update the model parameters (soil/rock wave velocities). For the forward modeling, the classic velocity-stress staggered-grid finite-difference method was used in combination with perfectly matched layer (PML) boundary conditions to solve the equations. For model updating, the gradient approach is used to minimize the residuals between the estimated responses obtained by forward simulation and the observed seismic data.

FORWARD MODELING OF 3D WAVE PROPAGATION

Three-dimensional elastic-wave propagation is modeled by a set of the first-order linear partial differential equations for isotropic materials. The first set of three equations governs particle velocities, whereas the second set of six equations governs the stress-strain tensors:

$$\left\{\begin{aligned} \dot{v}_x &= \frac{1}{\rho}\left(\frac{\partial\sigma_{xx}}{\partial x}+\frac{\partial\sigma_{xy}}{\partial y}+\frac{\partial\sigma_{xz}}{\partial z}\right)\\ \dot{v}_y &= \frac{1}{\rho}\left(\frac{\partial\sigma_{xy}}{\partial x}+\frac{\partial\sigma_{yy}}{\partial y}+\frac{\partial\sigma_{yz}}{\partial z}\right)\\ \dot{v}_z &= \frac{1}{\rho}\left(\frac{\partial\sigma_{xz}}{\partial x}+\frac{\partial\sigma_{yz}}{\partial y}+\frac{\partial\sigma_{zz}}{\partial z}\right)\end{aligned}\right., \tag{1}$$

$$\left\{\begin{aligned} \dot{\sigma}_{xx} &= (\lambda+2\mu)\frac{\partial v_x}{\partial x}+\lambda\left(\frac{\partial v_y}{\partial y}+\frac{\partial v_z}{\partial z}\right)\\ \dot{\sigma}_{yy} &= (\lambda+2\mu)\frac{\partial v_y}{\partial y}+\lambda\left(\frac{\partial v_x}{\partial x}+\frac{\partial v_z}{\partial z}\right)\\ \dot{\sigma}_{zz} &= (\lambda+2\mu)\frac{\partial v_z}{\partial z}+\lambda\left(\frac{\partial v_x}{\partial x}+\frac{\partial v_y}{\partial y}\right)\\ \dot{\sigma}_{xy} &= \mu\left(\frac{\partial v_x}{\partial y}+\frac{\partial v_y}{\partial x}\right)\\ \dot{\sigma}_{xz} &= \mu\left(\frac{\partial v_x}{\partial z}+\frac{\partial v_z}{\partial x}\right)\\ \dot{\sigma}_{yz} &= \mu\left(\frac{\partial v_y}{\partial z}+\frac{\partial v_z}{\partial y}\right)\end{aligned}\right., \tag{2}$$

where (v_x, v_y, v_z) is the particle velocity vector, $(\sigma_{xx}, \sigma_{yy}, \sigma_{zz}, \sigma_{xy}, \sigma_{xz}, \sigma_{yz})$ is the stress tensor, ρ is the mass density, μ and λ are the Lamé's coefficients, and the over-dot denotes a time derivative.

The classic velocity-stress staggered-grid finite-difference method (Virieux, 1986) was used to solve the equations in the time domain. The code was developed in MATLAB in which all stresses and particle velocities were calculated in matrix form at each time step and then advanced in the time domain. Shot parallelization was implemented to reduce the computer time. For example, the forward simulations for 32 shots were done simultaneously on our 32-core computer during inversion.

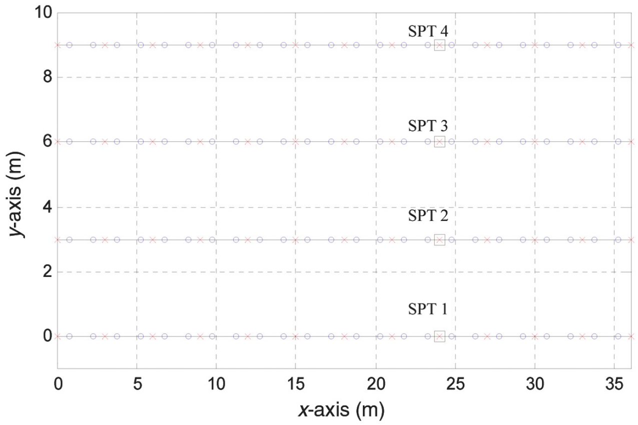

Figure 2. Test configuration used for synthetic and field experiments: source (cross), receiver (circle). The SPTs (square) are only for the field experiment.

An accurate free-surface boundary condition is implemented using the explicit finite-difference and image technique (Robertsson, 1996), whereas the perfectly matched layer (PML) (Komatitsch and Martin, 2007) is applied at the other boundaries. The PML is an added zone surrounding the domain of interest to absorb energy of outgoing waves, and it is an efficient method for domain truncation (Kallivokas et al., 2013). As an example, Figure 1 presents 3D wave propagation in a homogeneous medium with and without the PML conditions. The medium has V_S of 200 m/s and V_P of 400 m/s for the entire domain. The source is located on the free surface (depth $z = 0$). With the implementation of the PML, almost no reflected signals from boundaries are observed (Figure 1a), whereas significant reflected signals from boundaries are seen after 0.3 s (Figure 1b) without the PML.

GRADIENT-BASED MODEL UPDATE USING THE ADJOINT-STATE METHOD

For model updating, the steepest-descent method using the adjoint-state approach (Tarantola, 1984; Mora, 1987) is used to minimize the residuals between the estimated data from the forward

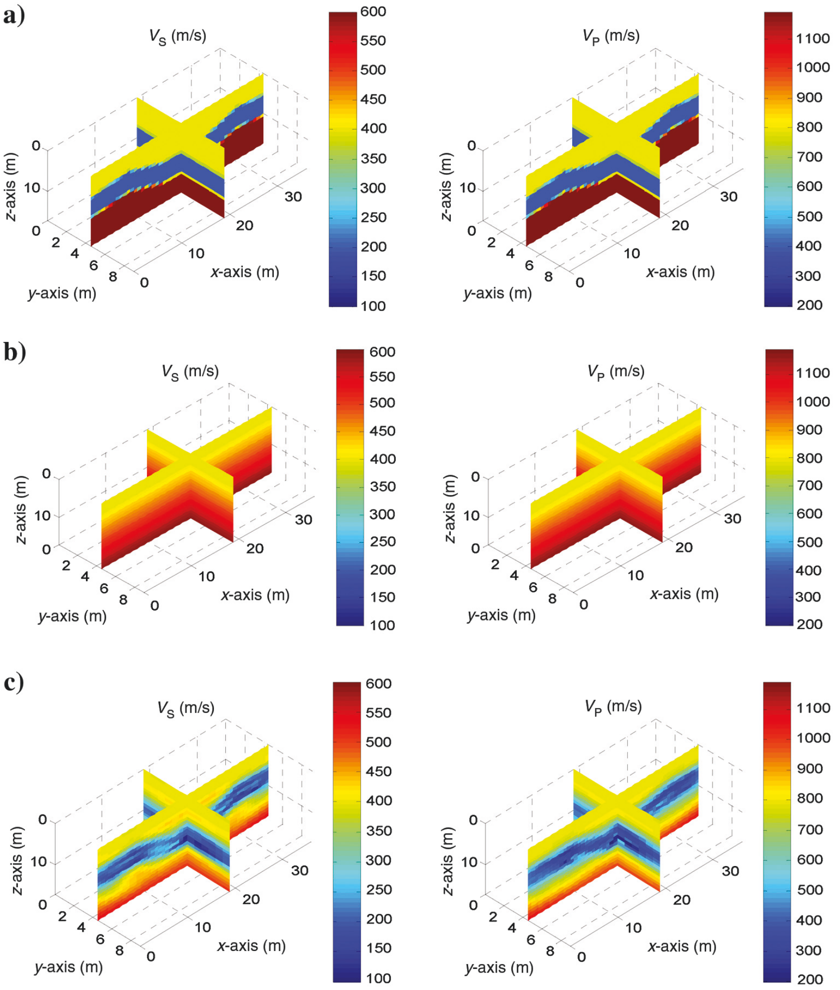

Figure 3. Synthetic model: distribution of V_S and V_P (m/s): (a) true model used to generate synthetic data for inversion analysis, (b) initial model used at the beginning of inversion, and (c) final inverted models, respectively.

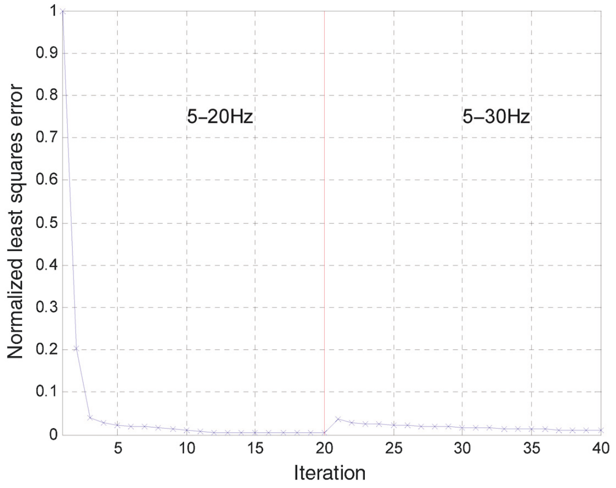

Figure 4. Synthetic model: normalized least-squares error versus the iteration number for both inversion runs at 5–20 and 5–30 Hz. The error defines the degree of match between the estimated and observed waveforms during the inversion analysis. The error increases at higher frequencies because the model is not yet appropriate to produce the recorded wave propagation of shorter wavelengths.

simulation and the observed (measured) waveform data. The misfit function is defined as a least-squares error $E(\mathbf{m})$:

$$E(\mathbf{m}) = \frac{1}{2}\Delta\mathbf{u}^t\Delta\mathbf{u},\quad \text{where } \Delta\mathbf{u} = \{\Delta u_{i,j}, i = 1, .., \mathrm{NS}, j = 1, .., \mathrm{NR}\}, \quad (3)$$

$\Delta u_{i,j}(t) = \int_0^t F_{i,j}(\mathbf{m},\tau)d\tau - \int_0^t d_{i,j}(\tau)d\tau$, $d_{i,j}$ and $F_{i,j}(\mathbf{m})$ are the time-domain observed data (vertical particle velocity) and estimated data associated with the model $\mathbf{m}$ (V_S and V_P of cells) from the forward simulation for shot i and receiver j. The term $\Delta\mathbf{u}$ is the displacement residual vector, which is a combination of residuals from all receivers and shots. NS and NR are the numbers of shots and receivers, respectively.

The gradients of the least-squares error E with respect to λ and μ can be calculated using the adjoint-state method in the time domain (Plessix, 2006; Butzer et al., 2013):

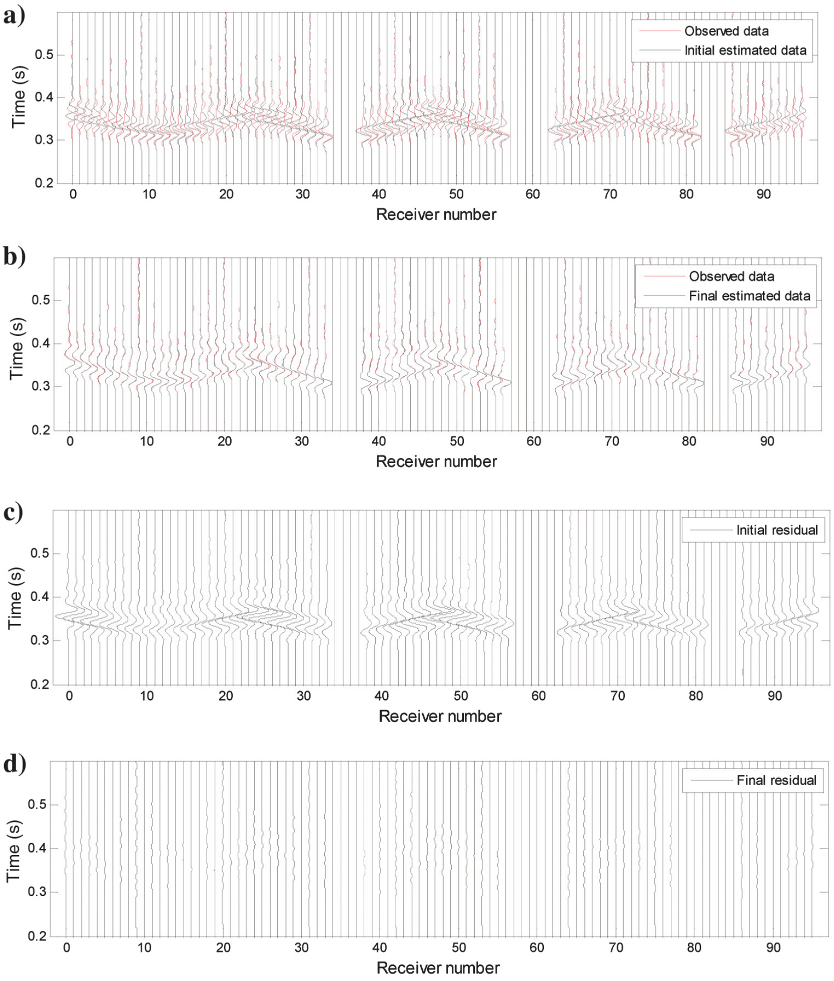

Figure 5. Synthetic model: waveform comparison for a sample shot: (a) observed data and estimated data associated with the initial model, (b) observed data and estimated data associated with the final inverted mode, (c) initial residual, and (d) final residual.

$$\delta\lambda = -\sum_{i=1}^{\mathrm{NS}}\int_0^T dt\left[\begin{array}{c}\left(\frac{\partial u_x}{\partial x}+\frac{\partial u_y}{\partial y}\right)\left(\frac{\partial \psi_x}{\partial x}+\frac{\partial \psi_y}{\partial y}\right)+\left(\frac{\partial u_x}{\partial x}+\frac{\partial u_z}{\partial z}\right)\left(\frac{\partial \psi_x}{\partial x}+\frac{\partial \psi_z}{\partial z}\right)\\ +\left(\frac{\partial u_y}{\partial y}+\frac{\partial u_z}{\partial z}\right)\left(\frac{\partial \psi_y}{\partial y}+\frac{\partial \psi_z}{\partial z}\right)\end{array}\right]$$

$$\delta\mu = -\sum_{i=1}^{\mathrm{NS}}\int_0^T dt\left[\begin{array}{c}\left(\frac{\partial u_x}{\partial y}+\frac{\partial u_y}{\partial x}\right)\left(\frac{\partial \psi_x}{\partial y}+\frac{\partial \psi_y}{\partial x}\right)+\left(\frac{\partial u_x}{\partial z}+\frac{\partial u_z}{\partial x}\right)\left(\frac{\partial \psi_x}{\partial z}+\frac{\partial \psi_z}{\partial x}\right)\\ +\left(\frac{\partial u_y}{\partial z}+\frac{\partial u_z}{\partial y}\right)\left(\frac{\partial \psi_y}{\partial z}+\frac{\partial \psi_x}{\partial z}\right)+2\left(\frac{\partial u_x}{\partial x}\frac{\partial \psi_x}{\partial x}+\frac{\partial u_y}{\partial y}\frac{\partial \psi_y}{\partial y}+\frac{\partial u_z}{\partial z}\frac{\partial \psi_z}{\partial z}\right)\end{array}\right] \tag{4}$$

where u_k and ψ_k are the forward and backward wavefields, with k denoting the spatial direction x, y, or z. Reversed-in-time displacement residuals are induced as multiple sources at all receiver locations for simulation of the backward wavefields. Forward wavefields (all time steps) and backward wavefields at the current time step of simulation (one time step) are stored in RAM for calculation of the gradients shot by shot.

Based on the wave velocity and Lamé's coefficient relationships: $V_\mathrm{P} = \sqrt{(\lambda + 2\mu)/\rho}$ and $V_\mathrm{S} = \sqrt{\mu/\rho}$, the gradients of the least-squares error E with respect to V_S and V_P are calculated as

$$\delta V_\mathrm{P} = 2\rho V_\mathrm{P}\delta\lambda$$
$$\delta V_\mathrm{S} = -4\rho V_\mathrm{S}\delta\lambda + 2\rho V_\mathrm{S}\delta\mu. \tag{5}$$

Gradient precondition is implemented to speed up the convergence rate. The precondition helps suppress large gradient values near the source and receiver positions to reduce inversion artifacts near the free surface. Specifically, a tapering radius from the source and receiver locations is used for gradually increasing the gradient scales from zero at the source/receiver locations to one at the outside of the circle. Furthermore, the gradients are linearly scaled with depth to resolve deeper structures (Ben-Hadj-Ali et al., 2008). Tikhonov regularization is also used to reduce inversion artifacts for reliability of inverted results. The regularized gradients are determined as

$$\delta^* V_\mathrm{P} = R_{V_\mathrm{P}}(LV_\mathrm{P}) + \delta V_\mathrm{P}$$
$$\delta^* V_\mathrm{S} = R_{V_\mathrm{S}}(LV_\mathrm{S}) + \delta V_\mathrm{S}, \tag{6}$$

where R_{V_S} and R_{V_P} are the V_S and V_P regularization factors: $R_{V_\mathrm{P}} = \beta\|\delta V_\mathrm{P}\|/\|LV_\mathrm{P}\|$, $R_{V_\mathrm{S}} = \beta\|\delta V_\mathrm{S}\|/\|LV_\mathrm{S}\|$ and L is the Laplacian matrix (discretization of 3D Laplacian operator). Several computations have been conducted in this study, and the value of β as 0.50 at the beginning and linearly decreased to 0.25 by the end of inversion analysis (for each inversion run) is selected because it produces good results for synthetic and field data.

Finally, V_S and V_P of cells at iteration $n+1$ are updated from iteration n as

$$V_\mathrm{P}^{n+1} = V_\mathrm{P}^{n} - \alpha_\mathrm{P}\delta^* V_\mathrm{P}$$
$$V_\mathrm{S}^{n+1} = V_\mathrm{S}^{n} - \alpha_\mathrm{S}\delta^* V_\mathrm{S}, \tag{7}$$

where α_P and α_S are the optimal step lengths that are estimated by parabola fitting (Nocedal and Wright, 2006). The gradient of V_P is scaled (e.g., $\max(\delta^* V_\mathrm{P})/\max(V_\mathrm{P}) = \max(\delta^* V_\mathrm{S})/\max(V_\mathrm{S})$) to determine one optimal step length, which is then scaled accordingly for α_P and α_S. During the inversion, the mass density is kept constant for the whole domain. Our efforts to invert the mass density have been shown to be unsuccessful because of dominant Rayleigh waves in surface-based waveform data that are not very sensitive to the mass density. The V_S and V_P of cells are updated iteratively, and a constraint is applied to V_P to maintain Poisson's ratio of all cells more than 0 and less than 0.45. The inversion analysis is stopped when no optimal step length is found (no better model) or the selected maximum number of iterations is reached.

APPLICATION ON SYNTHETIC DATA

Synthetic study allows data from a specific scenario to be generated for inversion. Synthetic model refers to an earth model whose velocity profile (i.e., V_S and V_P of cells) is assumed or known a

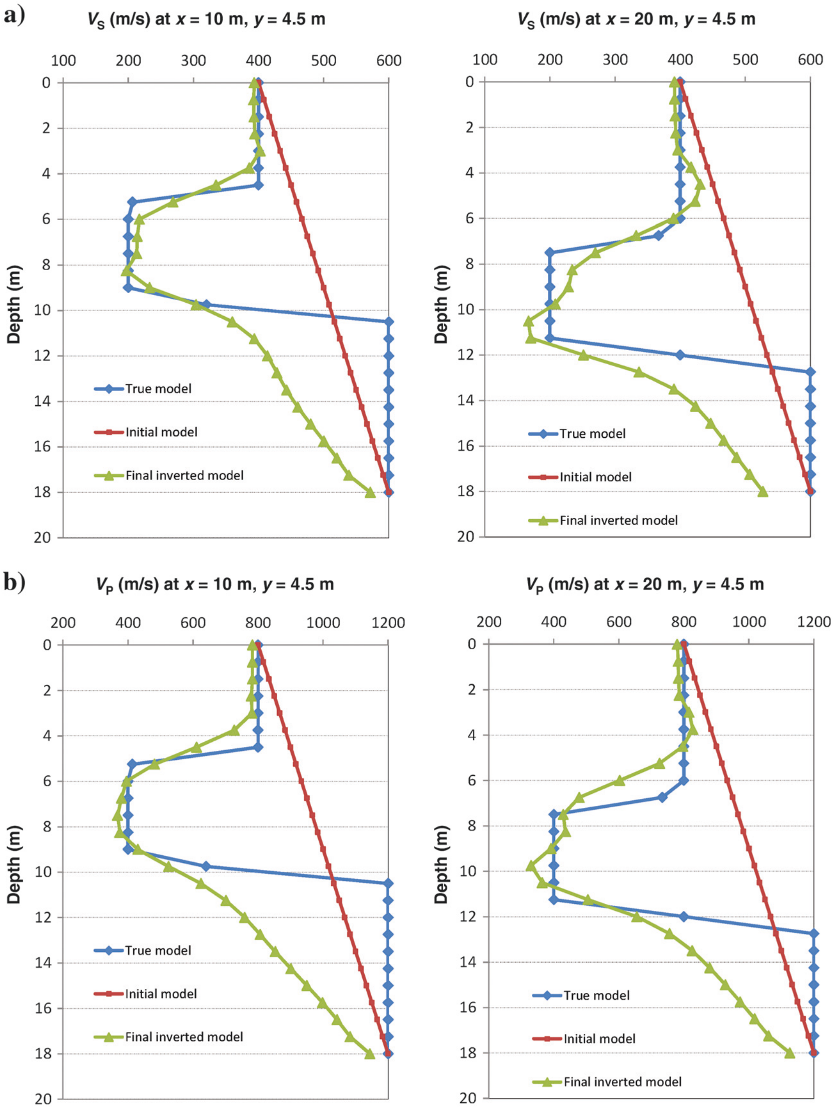

Figure 6. Synthetic model: comparison of (a) V_S and (b) V_P profiles at two locations.

priori. Using a known velocity structure, surface waveform data are calculated for an assumed test configuration (i.e., 2D uniform grids of shots and receivers as shown in Figure 2). These waveform data are then input to the inversion program as if the waveforms were acquired from a field test. Inverting the data produces 3D profiles of V_S and V_P structures, which lie directly below the receiver and shot area. Theoretically, the interpreted velocity profile should be the same as the true model.

To investigate the capability of the 3D FWI method, it was tested on a challenging model with high- and low-velocity layers. The synthetic model is 18 m deep, 36 m long, and 9 m wide, consisting of three soil layers (Figure 3a) with a low-velocity second layer. The three layers have V_S of 400, 200, and 600 m/s, and V_P of 800, 400, and 1200 m/s (twice that of V_S). The mass density is 1800 $\mathrm{kg/m^3}$ for the whole model. It represents the typical soil profile at the test site presented later for the field experiment.

For synthetic data generation, the test configuration (Figure 2) includes 96 receivers and 52 shots (sources) located in 2D uniform grids. The receiver grid is 4×24 at 3 and 1.5 m spacing in shorter and longer directions, respectively, and the source grid is 4×13 at 3 m spacing in both directions. The waveform data were created up to 30 Hz using the forward simulation (solutions of Equations 1 and 2) for 52 shots and recorded at the 96 receiver locations. A medium grid of 0.75 m vertical-force source and vertical receivers was used for the simulation. The Ricker wavelet of 15 Hz central frequency was used for the source signature, and the recorded time was 0.9 s with a sampling rate of 0.0003 s.

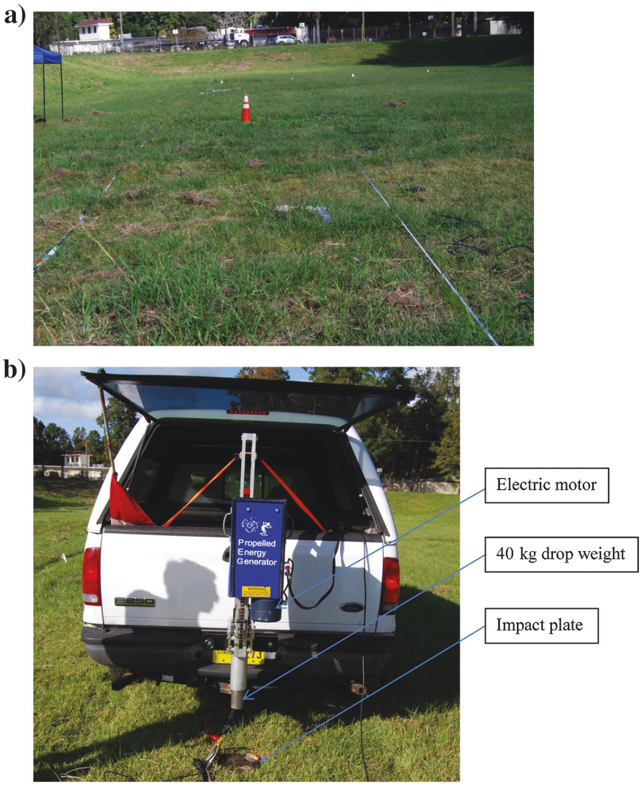

Figure 7. Field experiment: (a) test site and (b) PEG.

The inversion analysis began with a 1D initial model with V_S and V_P linearly increased with depth (Figure 3b), which could be obtained from analysis of Rayleigh-wave dispersion (see the case of the field data for a detailed discussion). The V_S profile increases from 400 m/s on the free surface (0 m depth) to 600 m/s at the bottom of the model (18 m depth), and the V_P is twice that of V_S. The mass density of 1800 $\mathrm{kg/m^3}$ for the whole model is assumed known and kept constant during inversion. It is noted that no prior information of the low-velocity layer is included in the initial model.

Two inversion runs were conducted from the data sets with two frequency bandwidths: 5–20 and 5–30 Hz with central frequencies of approximately 10 and 20 Hz, respectively. The same generated synthetic data set (using Ricker wavelet source of 15 Hz central frequency) was filtered through the two frequency bandwidths and were used as observed waveform data for the two inversion runs. The first run began with the lower frequency range (central frequency of 10 Hz) with the given initial model. The subsequent analysis was performed with the central frequency of 20 Hz using the final inverted results from the first run as the input model. During the inversions, the V_S and V_P of each cell were updated simultaneously. The optimal step length was calculated to update the model at every iteration. Both inversion runs were stopped after 20 iterations, when the change of the least-squares error was small (less than 1% from one to the next iteration). The complete analysis took approximately 17 h on a desktop computer (32 cores of 3.46 GHz each and 256 GB of memory).

The normalized least-squares error for all 40 iterations of the two inversion runs is shown in Figure 4. The error reduces approximately 98% from the first to the last iteration of the first inversion run, and it also reduces during the second inversion run. It is noted that the error increases when adding higher frequency components from 20 to 30 Hz because the model is not yet appropriate to produce the recorded wave propagation of shorter wavelengths.

Figure 5 shows the waveform comparison of a sample shot. The estimated waveforms associated with the initial model and the final inverted model are shown in Figure 5a and 5b, respectively, together with the observed data. Apparently, the final inverted model produces significant better match; the observed and final estimated data in Figure 5b are almost identical suggesting that the initial model is sufficent. No cycle skipping was observed for any shots. Residuals associated with the initial and final inverted models are shown in Figure 5c and 5d, respectively. The initial residuals are very large (Figure 5c), whereas the final residuals are close to zero for all channels (Figure 5d).

The final analyzed results (5–30 Hz) are shown in Figure 3c. It is evident that the inverted profile is very similar to the true profile (Figure 3a). The layer interfaces were accurately characterized. True V_S and V_P values of the three layers were recovered, including the low-velocity second layer. For detailed comparison, the V_S and V_P profiles of the inverted model at two locations are plotted in Figure 6, together with these of the true model and the initial model. The inverted profiles are quite different from the initial profiles, suggesting considerable parameter change during inversion analysis. A good match is found between the inverted and true profiles, except the sharp interface between the bottom two layers. This is the limitation of the standard Tikhonov regularization used in the waveform analysis (Equation 6). It always generates smooth inverted velocity models. Nevertheless, the 3D FWI method shows great potential for characterization of challenging site conditions with variable high- and low-velocity layers.

APPLICATION ON FIELD DATA

Obtaining promising results on synthetic waveform data set, the presented 3D FWI method was then applied to field experimental data. The test site was a dry retention pond in Gainesville, Florida, USA (Figure 7a). The same test configuration of 96 receivers and 52 shots (Figure 3) was used for the field seismic survey. The receiver grid was 4 × 24, and the source grid was 4 × 13. The seismic wavefields were generated by a propelled energy generator (PEG, 40 kg model) as shown in Figure 7b, and simultaneously recorded by 48 4.5 Hz vertical geophones in two stages. In stage one, the 48 geophones were placed at the first half of the receiver grid (the first two lines, 24 geophones each line) and 52 shots were conducted for the entire source grid. In stage two, the 48 geophones were placed at the second half of the receiver grid (the last two lines, 24 geophones each line), and 52 shots were repeated. The PEG generated the same impact load (the same drop weight and height), and the trigger was attached to the impact plate to activate the seismograph at the same time (the same delayed time in the recorded data) for every shot location. The collected data from the two stages were combined to produce 96-channel shot gathers. The recorded time was 0.7 s with the sampling rate of 0.0005 s. Four standard penetration tests (SPTs) were also conducted at a distance of 24 m on each geophone line for verification of the seismic results.

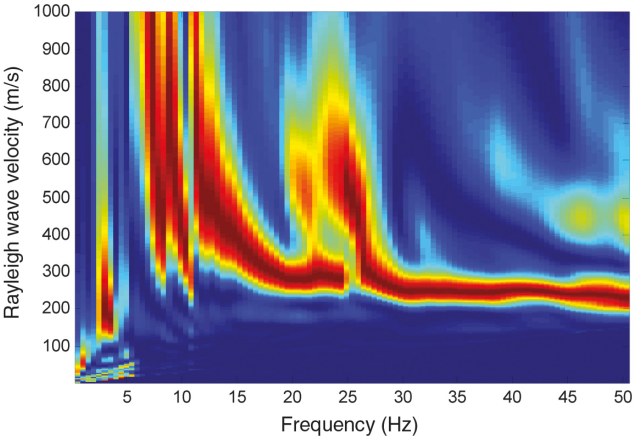

Figure 9. Field experiment: spectral analysis of measured data for one sample shot and one line of 24 geophones.

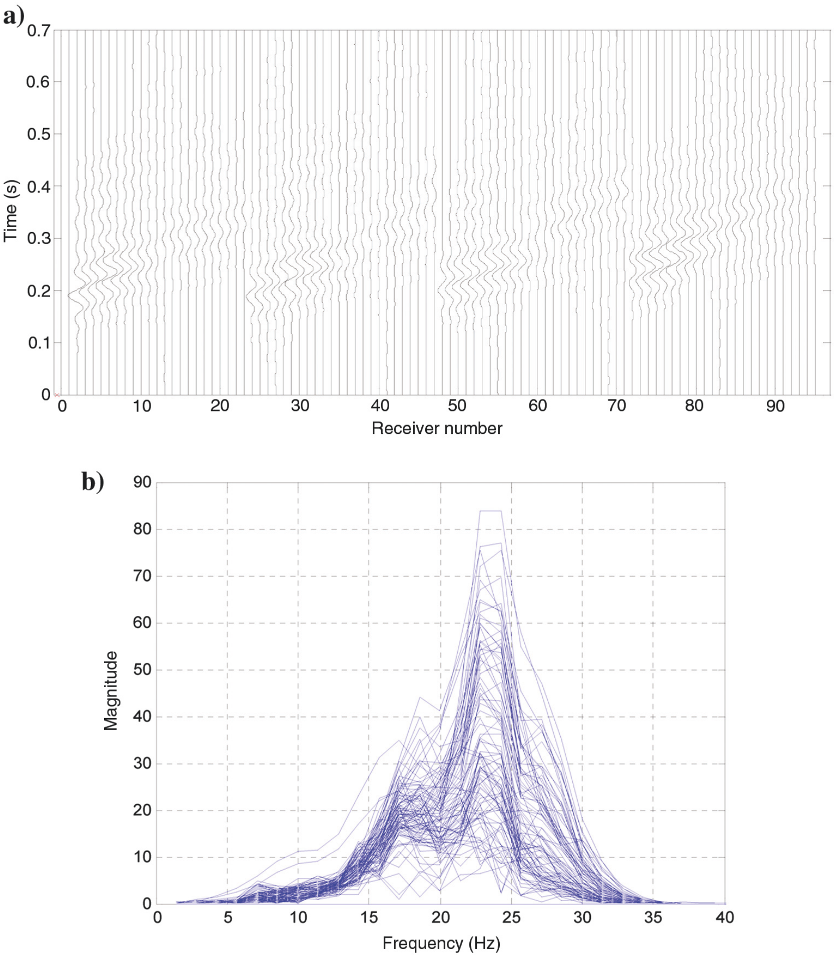

Figure 8. Field experiment: (a) measured data for a sample shot and (b) corresponding spectrum. Data are high-cut filtered to remove frequency components of greater than 30 Hz.

As an example, the measured data combined from the two stages for the first shot are shown in Figure 8a. The data were high-cut filtered to remove frequency components larger than 30 Hz. Consistent wave magnitudes and propagation patterns are observed. The corresponding frequency spectrum, whose central frequency is approximately 22 Hz, is shown in Figure 8b.

For inversion analysis, issues associated with initial models, attenuation of the measured data, and unknown impact forces (source signatures) were addressed. An appropriate initial model is required to avoid cycle skipping that produces inaccurate local solutions. The initial model could be generated by using global inversion techniques, such as the genetic algorithm (Tran and Hiltunen, 2012a) or simulated annealing (Tran and Hiltunen, 2012b) on full-waveform data. This approach likely produces the global solution but requires significant computer time. Alternatively, from the synthetic study, the 1D initial model of increasing wave velocities with depth was sufficient to invert the profile with variable high- and low-velocity layers. Such a 1D initial model was estimated via spectral analysis of the measured data. Figure 9 shows the spectral image of the measured data for one sample shot and one line of 24 geophones. The Rayleigh-wave velocities V_{R} were determined from 250 to 400 m/s at the frequency range of 12–50 Hz. The V_{R} at the surface associated with high frequencies was known, approximately 250 m/s. The half-space was assumed starting at the depth of a half-maximum wavelength ($0.5 \times \text{wavelength} = 0.5 \times \text{velocity}/\text{frequency} = 0.5 \times 400/12 = 16.6$ m) and having a constant V_{R} of 400 m/s. Because V_{S} is similar to Rayleigh-wave velocity, the initial model was established having V_{S} increasing with depth from 250 m/s at the surface to 400 m/s at the bottom of the model (Figure 10a). The depth of the model was assumed to be a half of the longer dimension of the test configuration as 18 m (good signal coverage). The value V_{P} was calculated from V_{S}, and we assumed

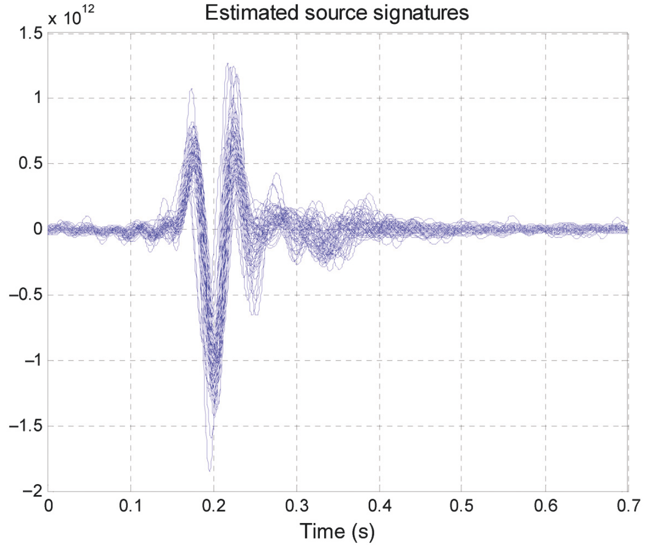

Figure 11. Field experiment: estimated source signatures for all 52 shots. The estimated source signatures were obtained by deconvolution of measured data with the Green's function.

Figure 10. Field experiment: distribution of V_{S} and V_{P} (m/s): (a) initial model used at the beginning of inversion and (b) final inverted models at 5–30 Hz.

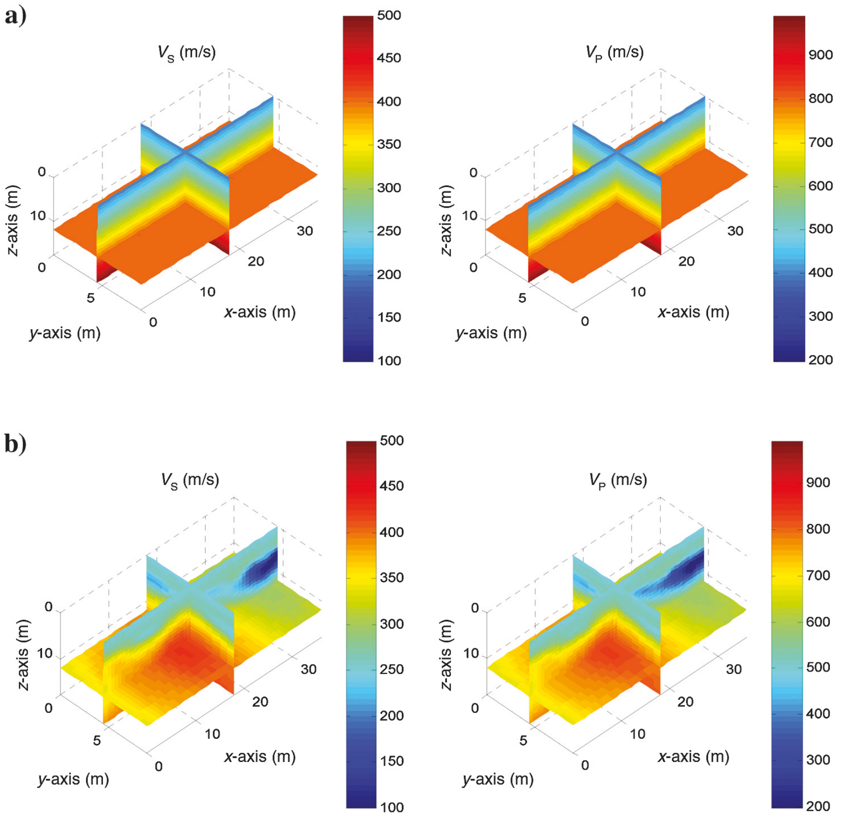

a Poisson's ratio of 1/3 for the entire medium, which was taken as the middle value of the 1/4–1/2 range for typical soils. The mass density was assumed as 1800 $\mathrm{kg/m^3}$ for the whole medium and kept constant during inversion.

To further avoid local solutions, the inversion analysis was done in a sequence of increasing frequencies because lower frequency data (large wavelengths) require fewer details in the initial models. Two inversion runs were conducted for filtered data sets at two frequency bandwidths: 5–20 and 5–30 Hz with central frequencies of approximately 12 and 22 Hz, respectively. The first run at 5–20 Hz began with the initial model shown in Figure 10a, and the second run began with the inverted result of the first run.

Attenuation of the field data due to radiation damping (geometric spreading) and material damping (anelasticity) must be accounted in the waveform analysis (Groos et al., 2014). The geometric spreading attenuation was already included in the 3D forward simulation, in which the field source impact was modeled as a concentrated dynamic load. To compensate for the attenuation due to material damping, modeled waveform data (estimated data) were adjusted by an offset-dependent correction factor of the form $y(r) = A \cdot r^{\alpha}$ (Schäfer et al., 2012), where r is the source-receiver offset and the factor A and exponent α were determined with an iterative

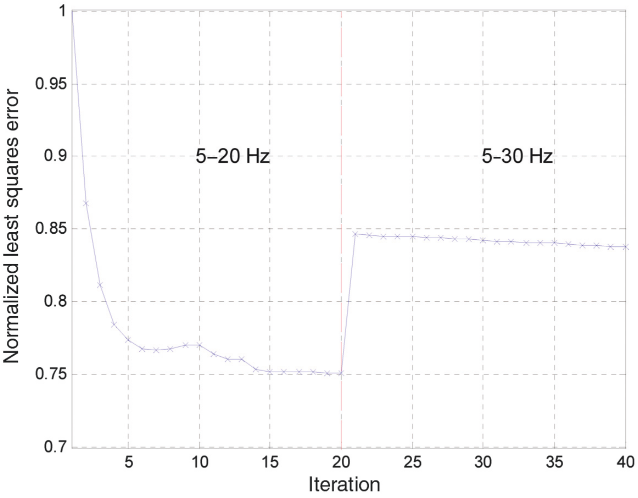

Figure 13. Field experiment: normalized least-squares error versus the inversion iteration number for both inversion runs at 5–20 and 5–30 Hz. The error defines the degree of match between the estimated and observed waveforms during the inversion analysis. The error increases at higher frequencies because the model is not yet appropriate to produce the recorded wave propagation of shorter wavelengths.

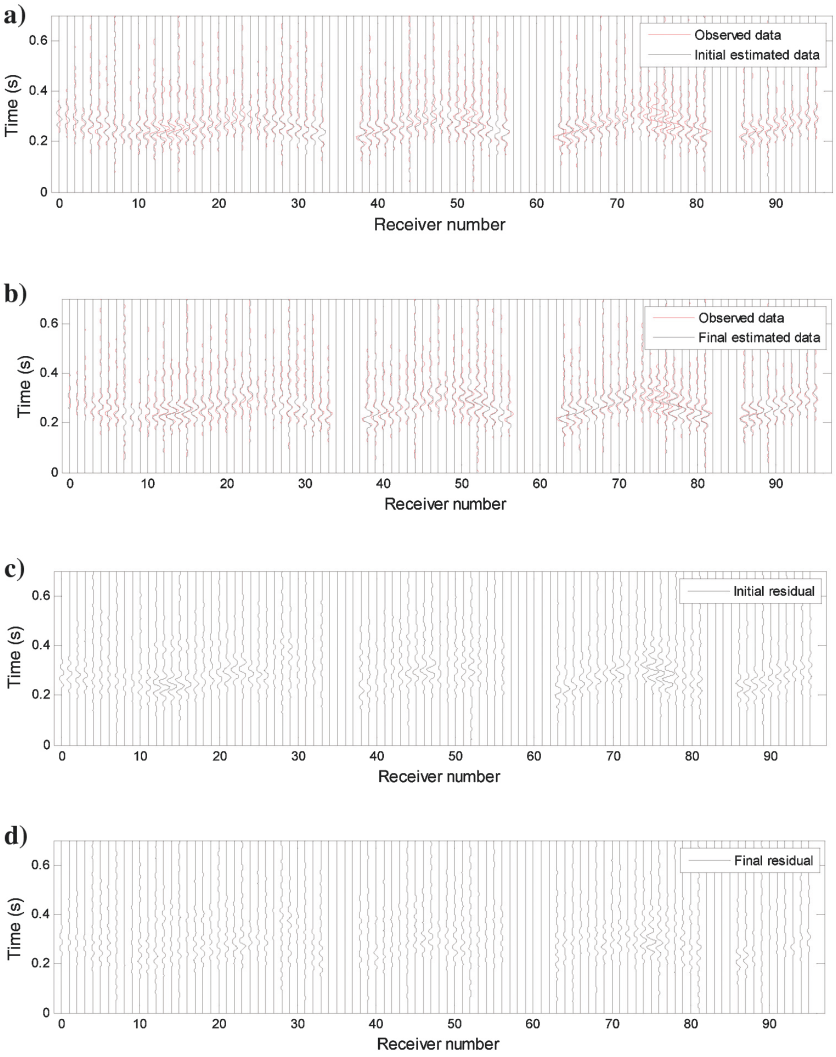

Figure 12. Field experiment: waveform comparison for a sample shot: (a) observed data and estimated data associated with the initial model, (b) observed data and estimated data associated with the final inverted mode, (c) initial residual, and (d) final residual.

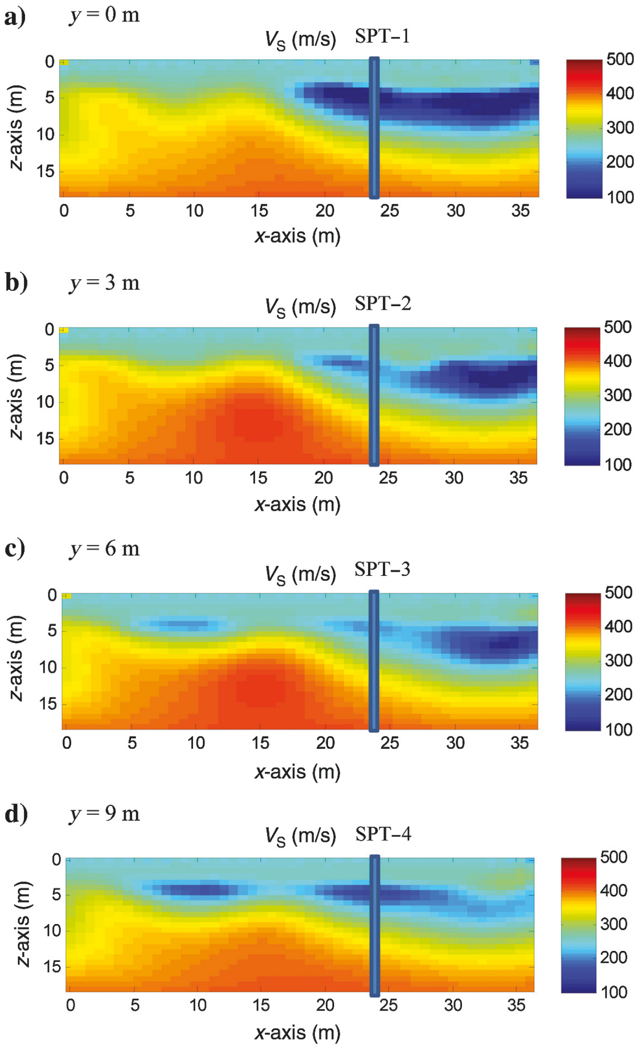

Figure 14. Field experiment: inverted V_S and SPT locations along four receiver lines at $y = 0$, 3, 6, and 9 m.

least-squares inversion that minimizes the energy of the waveform residuals. The correction factor represents an average attenuation for the entire data set for all receivers and all shots.

For forward simulations, accurate source signatures are required. If the source signatures are inaccurate, the estimated data could be significantly off in phase and magnitude to those of the measured data. This may lead to undesired local solutions and inversion artifacts. The source estimation approach (Tran and Luke, 2017) developed for a 2D FWI method was used herein. The estimated source was obtained by deconvolution of the measured data with the Green's function, which were explicitly calculated by forward simulation with an assumed source. The assumed source was a Ricker wavelet having the same central frequency of analyzing data (e.g., 12 or 22 Hz), unit magnitude, and a delayed time of 0.2 s. It is noted that the magnitude and delayed time of the assumed source are different from those of estimated source signatures. The source signatures associated with the initial model for 52 shots are shown in Figure 11. They are similar in phase and magnitude, showing the consistency of the PEG source. Because the Green's function was changing during inversion due to the updated material properties V_S and V_P, the estimated source signatures were determined (updated) at the beginning of each inversion iteration.

The $18 \times 36 \times 9$ m (depth × length × width) medium was divided into 13,824 cells of $0.75 \times 0.75 \times 0.75$ m. The cell size of 0.75 m was selected as a half of the smaller geophone spacing (1.5 m), and it was used for both inversion runs. Similar to the synthetic study, the optimal step length was determined for each iteration to update the model. The V_S and V_P of the cells were updated simultaneously, and both inversion runs stopped at 20 iterations. The complete analysis took approximately 20 h on the same computer used for the synthetic data analysis. The third inversion run with higher frequency data at 5–40 Hz was also attempted, but the least-squares error did not decrease. The inverted result was almost the same as that of the run at 5–30 Hz, and it is not included in this paper.

Figure 12 shows the waveform comparison for a sample shot. The estimated waveforms associated with the initial model and final inverted model are shown in Figure 12a and 12b, respectively, together with the observed data. The final inverted model produces a better waveform match than the initial model. The observed and the final estimated data in Figure 12b agree well, and no cycle skiping is observed, suggesting that the 1D initial model was sufficent. Residuals associated with the initial and final inverted models are shown in Figure 12c and 12d, respectively, and the final residuals are smaller than the initial residuals.

The normalized least-squares error for all 40 iterations of the two inversion runs is shown in Figure 13. Unlike the synthetic study, the error for field data only reduces by approximately 25% from the first to the last iteration of the first run and it reduces less for the second run because the selected initial model is closer to the true profile than that of the synthetic case. The initial residuals of the field data (Figure 12c) are much smaller than those of the synthetic data (Figure 5c), thus it is more difficult to reduce. This is also due to the material damping that could not be completely addressed by the proposed offset-dependent correction and resulted in discrepancy between measured and estimated data (remaining in the final residuals).

The final inverted model for data at 5–30 Hz is shown in Figure 10b. The V_S profile consists of soft soil layers ($V_S \sim 100 - 300$ m/s) with embedded low-velocity zones at shallow depths, underlain by a stiffer weather limestone layer ($V_S \sim 400 - 500$ m/s). The V_P profile is consistent with the V_S profile. For a better illustration of lateral variation, Figure 14 shows V_S profiles along four receiver lines at $y = 0$, 3, 6, and 9 m, together with the four SPT locations. Consistent variation of the soil layers is observed along the y-direction.

A comparison between the initial and inverted V_S profiles and SPT N-values at four locations is shown in Figure 15. The SPTs were conducted down to an approximately 21 m depth. The inverted profiles are quite different from the initial profiles, particularly at the low-velocity zones, suggesting that considerable V_S was changed during the inversion analysis. The seismic and SPT results are generally consistent. Both show softer materials from 0 to 5 m in depth, linearly increasing stiffness with depth from 5 to 10 m in depth, and stiffer materials at less than 10 m depth. Interestingly, the low-velocity zone at approximately 5 m in depth identified by the 3D FWI analysis is confirmed by the SPT results, particularly at SPT-3 and SPT-4.

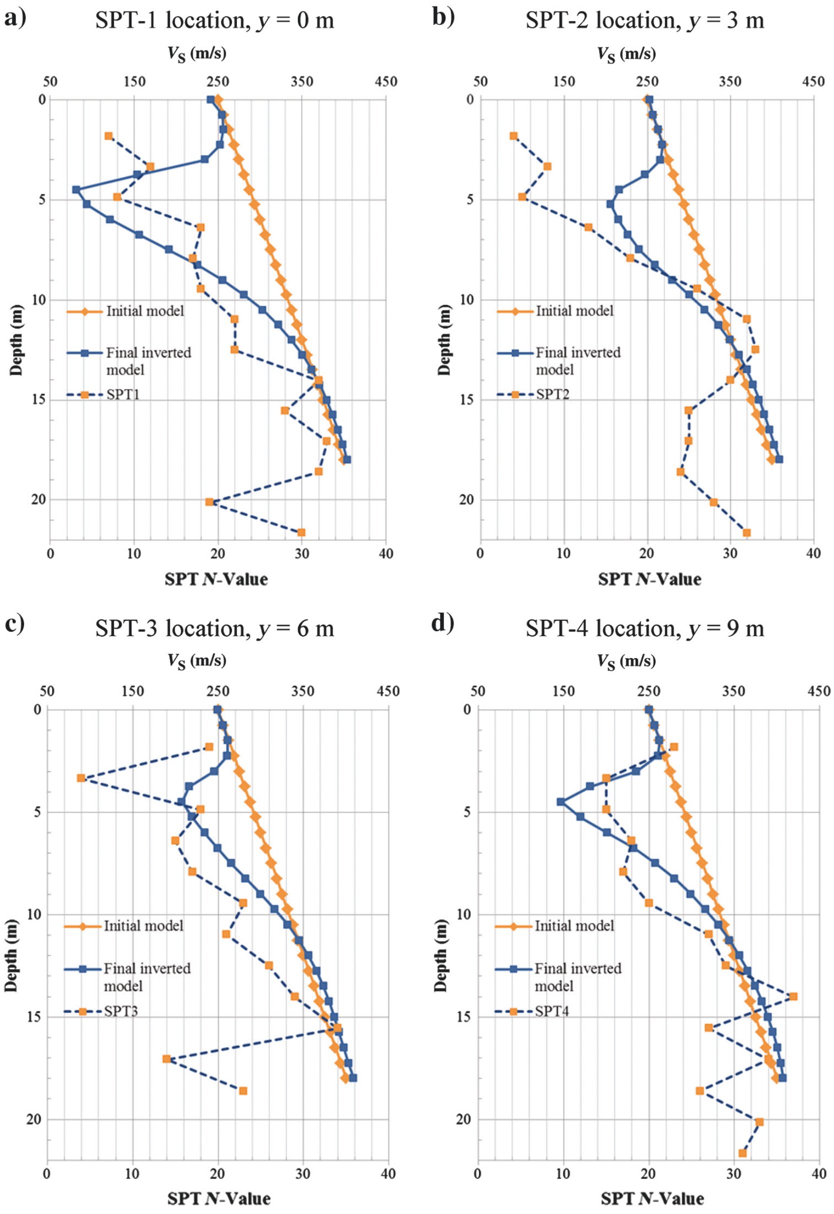

Figure 15. Comparison between V_S and SPT N-values at the four invasive test locations.

CONCLUSION

A 3D FWI method is presented for geotechnical site characterization. The method is based on a solution of 3D elastic-wave equations for forward modeling to simulate wave propagation and a cross-adjoint gradient approach for model updating to extract material property. Seismic wavefields are acquired from geophysical testing using sensors and sources located in uniform 2D grids on the ground surface and then inverted for the extraction of 3D subsurface wave velocity structures. The method was applied to synthetic and field data sets. The results from synthetic data set suggest that the waveform analysis can characterize variable high- and low-velocity subsurface layers. For the field data, V_S and V_P of 3D variable soil layers are characterized. There also appears to be good consistency between the V_S and SPT N-values, including the identification of a buried low-velocity zone. In addition, the 3D FWI method is computationally practical; the presented results were all obtained within 20 h on a standard desktop computer.

ACKNOWLEDGMENTS

This study was financially supported by the National Science Foundation, grant no. CMMI-1637557. The authors would like to thank the Florida Department of Transportation and the State Materials Office in Gainesville, Florida, for providing access to the test site and conducting the SPT tests.

REFERENCES

Askan, A., V Akcelik, J. Bielak, and O. Ghattas, 2007, Full waveform inversion for seismic velocity and anelastic losses in heterogeneous structures: Bulletin of the Seismological Society of America, **97**, 1990–2008, doi: 10.1785/0120070079.

Ben-Hadj-Ali, H., S. Operto, and J. Virieux, 2008, Velocity model building by 3D frequency-domain, full-waveform inversion of wide-aperture seismic data: Geophysics, **73**, no. 5, VE101–VE117, doi: 10.1190/1.2957948.

Ben-Hadj-Ali, H., S. Operto, and J. Virieux, 2011, An efficient frequency-domain full waveform inversion method using simultaneous encoded sources: Geophysics, **76**, no. 4, R109–R124, doi: 10.1190/1.3581357.

Brenders, A. J., and R. G. Pratt, 2007, Full waveform tomography for lithospheric imaging: Results from a blind test in a realistic crustal model: Geophysical Journal International, **168**, 133–151, doi: 10.1111/j.1365-246X.2006.03156.x.

Bretaudeau, F., R. Brossier, D. Leparoux, O. Abraham, and J. Virieux, 2013, 2D elastic full-waveform imaging of the near-surface: Application to synthetic and physical modelling data sets: Near Surface Geophysics, **11**, 307–316.

Brossier, R., S. Operto, and J. Virieux, 2010, Which data residual norm for robust elastic frequency-domain full waveform inversion?: Geophysics, **75**, no. 3, R37–R46, doi: 10.1190/1.3379323.

Butzer, S., A. Kurzmann, and T. Bohlen, 2013, 3D elastic full-waveform inversion of small-scale heterogeneities in transmission geometry: Geophysical Prospecting, **61**, 1238–1251, doi: 10.1111/1365-2478.12065.

Castellanos, C., L. Métivier, S. Operto, R. Brossier, and J. Virieux, 2015, Fast full waveform inversion with source encoding and second-order optimization methods: Geophysical Journal International, **200**, 720–744, doi: 10.1093/gji/ggu427.

Cheong, S., S. Pyun, and C. Shin, 2006, Two efficient steepest-descent algorithms for source signature-free waveform inversion: Journal of Seismic Exploration, **14**, 335–348.

Epanomeritakis, I., V. Akcelik, O. Ghattas, and J. Bielak, 2008, A Newton-CG method for large-scale three-dimensional elastic full waveform seismic inversion: Inverse Problems, **24**, 034015, doi: 10.1088/0266-5611/24/3/034015.

Fathi, A., L. Kallivokas, and B. Poursartip, 2015, Full waveform inversion in three-dimensional PML-truncated elastic media: Computer Methods in Applied Mechanics and Engineering, **296**, 39–72, doi: 10.1016/j.cma.2015.07.008.

Fathi, A., B. Poursartip, K. H. Stokoe, and L. Kallivokas, 2016, Three-dimensional P-and S-wave velocity profiling of geotechnical sites using full-waveform inversion driven by field data: Soil Dynamics and Earthquake Engineering, **87**, 63–81, doi: 10.1016/j.soildyn.2016.04.010.

Fichtner, A., B. Kennett, H. Igel, and H. P. Bunge, 2009, Full seismic waveform tomography for upper-mantle structure in the Australasian region using adjoint methods: Geophysical Journal International, **179**, 1703–1725, doi: 10.1111/j.1365-246X.2009.04368.x.

Gélis, C., J. Virieux, and G. Grandjean, 2007, Two-dimensional elastic waveform inversion using Born and Rytov formulations in the frequency domain: Geophysical Journal International, **168**, 605–633, doi: 10.1111/j.1365-246X.2006.03135.x.

Groos, L., M. Schäfer, T. Forbriger, and T. Bohlen, 2014, The role of attenuation in 2D full-waveform inversion of shallow-seismic body and Rayleigh waves: Geophysics, **79**, no. 6, R247–R261, doi: 10.1190/geo2013-0462.1.

Ha, W., S. Kang, and C. Shin, 2015, 3D Laplace-domain waveform inversion using a low-frequency time-domain modeling algorithm: Geophysics, **80**, no. 1, R1–R13, doi: 10.1190/geo2013-0332.1.

Kallivokas, L., A. Fathi, S. Kucukcoban, K. H. Stokoe, J. Bielak, and O. Ghattas, 2013, Site characterization using full waveform inversion: Soil Dynamics and Earthquake Engineering, **47**, 62–82.

Kamatitsch, D., and R. Martin, 2007, An unsplit convolutional perfectly matched layer improved at grazing incidence for the seismic wave equation: Geophysics, **72**, no. 5, SM155–SM167, doi: 10.1190/1.2757586.

Köhn, D., T. Meier, M. Fehr, D. De Nil, and M. Auras, 2016, Application of 2D elastic Rayleigh waveform inversion to ultrasonic laboratory and field data: Near Surface Geophysics, **14**, 461–476.

Métivier, L., F. Bretaudeau, R. Brossier, S. Operto, and J. Virieux, 2014, Full waveform inversion and the truncated Newton method: Quantitative imaging of complex subsurface structures: Geophysical Prospecting, **62**, 1353–1375, doi: 10.1111/1365-2478.12136.

Mora, P., 1987, Nonlinear twodimensional elastic inversion of multioffset seismic data: Geophysics, **52**, 1211–1228, doi: 10.1190/1.1442384.

Nguyen, D. T., K. T. Tran, and M. McVay, 2016, Evaluation of unknown foundations using surface-based full waveform tomography: Journal of Bridge Engineering, **21**, 04016013-1–04016013-10, doi: 10.1061/(ASCE)BE.1943-5592.0000866.

Nocedal, J., and S. Wright, 2006, Numerical optimization: Springer.

Operto, S., Y. Gholami, V. Prieux, A. Ribodetti, R. Brossier, L. Métivier, and J. Virieux, 2013, A guided tour of multi-parameter full waveform inversion for multicomponent data: From theory to practice: The Leading Edge, **32**, 1040–1054, doi: 10.1190/tle32091040.1.

Park, C., R. D. Miller, and J. B. Xia, 1999, Multichannel analysis of surface waves: Geophysics, **64**, 800–808, doi: 10.1190/1.1444590.

Plessix, R., 2009, Three-dimensional frequency-domain full-waveform inversion with an iterative solver: Geophysics, **74**, no. 6, WCC149–WCC157, doi: 10.1190/1.3211198.

Plessix, R. E., 2006, A review of the adjoint-state method for computing the gradient of a functional with geophysical applications: Geophysical Journal International, **167**, 495–503, doi: 10.1111/j.1365-246X.2006.02978.x.

Pratt, R. G., C. Shin, and G. J. Hicks, 1998, Gauss-Newton and full Newton methods in frequency-space seismic waveform inversion: Geophysical Journal International, **133**, 341–362, doi: 10.1046/j.1365-246X.1998.00498.x.

Prieux, V., R. Brossier, Y. Gholami, S. Operto, J. Virieux, O. Barkved, and J. Kommedal, 2011, On the footprint of anisotropy on isotropic full waveform inversion: The Valhall case study: Geophysical Journal International, **187**, 1495–1515, doi: 10.1111/j.1365-246X.2011.05209.x.

Prieux, V., R. Brossier, S. Operto, and J. Virieux, 2013, Multi-parameter full waveform inversion of multicomponent OBC data from Valhall — Part 1: Imaging compressional wave speed, density and attenuation: Geophysical Journal International, **194**, 1640–1664, doi: 10.1093/gji/ggt177.

Ravaut, C., S. Operto, L. Improta, J. Virieux, A. Herrero, and P. Dell'Aversana, 2004, Multiscale imaging of complex structures from multifold wide-aperture seismic data by frequency-domain full-wavefield tomography: Application to a thrust belt: Geophysical Journal International, **159**, 1032–1056, doi: 10.1111/j.1365-246X.2004.02442.x.

Robertsson, J. O. A., 1996, A numerical free-surface condition for elastic/viscoelastic finite-difference modeling in the presence of topography: Geophysics, **61**, 1921–1934, doi: 10.1190/1.1444107.

Romdhane, A., G. Grandjean, R. Brossier, F. Rejiba, S. Operto, and J. Virieux, 2011, Shallow-structure characterization by 2D elastic full-waveform inversion: Geophysics, **76**, no. 3, R81–R93, doi: 10.1190/1.3569798.

Rosenbrock, H., 1960, An automatic method for finding the greatest or least value of a function: The Computer Journal, **3**, 175–184, doi: 10.1093/comjnl/3.3.175.

Schäfer, M., L. Groos, T. Forbriger, and T. Bohlen, 2012, On the effects of geometrical spreading corrections for a 2D full waveform inversion of recorded shallow seismic surface waves: 74th Annual International Conference and Exhibition, EAGE, Extended Abstracts, doi: 10.3997/2214-4609.20148327.

Sears, T., S. Singh, and P. Barton, 2008, Elastic full waveform inversion of multi-component OBC seismic data: Geophysical Prospecting, **56**, 843–862, doi: 10.1111/j.1365-2478.2008.00692.x.

Sheen, D. H., K. Tuncay, C. E. Baag, and P. J. Ortoleva, 2006, Time domain Gauss-Newton seismic waveform inversion in elastic media: Geophysical Journal International, **167**, 1373–1384, doi: 10.1111/j.1365-246X.2006.03162.x.

Shipp, R. M., and S. C. Singh, 2002, Two-dimensional full wavefield inversion of wide-aperture marine seismic streamer data: Geophysical Journal International, **151**, 325–344, doi: 10.1046/j.1365-246X.2002.01645.x.

Sirgue, L., O. Barkved, J. Dellinger, J. Etgen, U. Albertin, and J. Kommedal, 2010, Full waveform inversion: The next leap forward in imaging at Valhall: First Break, **28**, 65–70, doi: 10.3997/1365-2397.2010012.

Sullivan, B., K. T. Tran, and B. Logston, 2016, Characterization of abandoned mine voids under roadway using land-streamer seismic waves: Journal of Transportation Research Board, **2580**, 71–79.

Tarantola, A., 1984, Inversion of seismic reflection data in the acoustic approximation: Geophysics, **49**, 1259–1266, doi: 10.1190/1.1441754.

Tran, K. T., and D. R. Hiltunen, 2012a, One-dimensional inversion of full waveform using genetic algorithm: Journal of Environmental and Engineering Geophysics, **17**, 197–213.

Tran, K. T., and D. R. Hiltunen, 2012b, Two-dimensional inversion of full waveform using simulated annealing: Journal of Geotechnical and Geoenvironmental Engineering, **138**, 1075–1090, doi: 10.1061/(ASCE)GT.1943-5606.0000685.

Tran, K. T., and B. Luke, 2017, Full waveform tomography to resolve desert alluvium: Soil Dynamics and Earthquake Engineering, **99**, 1–8, doi: 10.1016/j.soildyn.2017.04.018.

Tran, K. T., and M. McVay, 2012, Site characterization using Gauss-Newton inversion of 2-D full seismic waveform in time domain: Soil Dynamics and Earthquake Engineering, **43**, 16–24, doi: 10.1016/j.soildyn.2012.07.004.

Tran, K. T., M. McVay, M. Faraone, and D. Horhota, 2013, Sinkhole detection using 2-D full seismic waveform tomography: Geophysics, **78**, no. 5, R175–R183, doi: 10.1190/geo2013-0063.1.

Vigh, D., J. Kapoor, N. Moldoveanu, and H. Li, 2011, Breakthrough acquisition and technologies for subsalt imaging: Geophysics, **76**, no. 5, WB41–WB51, doi: 10.1190/geo2010-0399.1.

Vigh, D., N. Moldoveanu, K. Jiao, W. Huang, and J. Kapoor, 2013, Ultralong offset data acquisition can complement full-waveform inversion and lead to improved subsalt imaging: The Leading Edge, **32**, 1116–1122, doi: 10.1190/tle32091116.1.

Virieux, J., 1986, P-SV wave propagation in heterogeneous media: Velocity-stress finite-difference method: Geophysics, **51**, 889–901, doi: 10.1190/1.1442147.

Vireux, J., and S. Operto, 2009, An overview of full-waveform inversion in exploration geophysics: Geophysics, **74**, no. 6, WCC1–WCC26, doi: 10.1190/1.3238367.

Warner, M., A. Ratcliffe, T. Nangoo, J. Morgan, A. Umpleby, and N. Shah, 2013, Anisotropic 3D full-waveform inversion: Geophysics, **78**, no. 2, R59–R80, doi: 10.1190/geo2012-0338.1.